

Dynamics for Biomimetic Continuum Arms: A Modal Approach

Isuru S. Godage, David T. Branson, Emanuele Guglielmino,
 Gustavo A. Medrano-Cerda, and Darwin G. Caldwell

Abstract—This paper presents an improved 3D dynamic model based on mode shape functions for biomimetic continuum robotic arms intended for underwater operation. It is an extension to the dynamic model proposed in the author's previous work to incorporate angular moments and hydrodynamic forces such as buoyancy, lift, and drag. The proposed model is based on an accurate kinematic model and gives an enhanced insight into practical mechanics. Also, it can be generalized for any variable length continuum arm to include external forces. A feedback control structure in the joint space is also implemented for increased performance of the continuum arm. Numerical results demonstrate underwater effects for spatial bending and pure elongations/contractions. The model carefully accounts for mechanical constraints in the joint space to yield physically accurate results.

I. INTRODUCTION

With the availability of increasingly advanced technologies many types of continuum robotic arms (also known as hyper redundant, and continuous backbone robots) are being developed and analyzed [1]. They provide a challenging alternative to traditional rigid link robots for many potential applications including minimal invasive surgeries and operations in unstructured environments. The recent trend for continuum robotics is inspired by natural examples such as elephant trunks, octopus arms, and lizard tongues that work on the muscular hydrostatic principle [2]. Without skeletal constraints, these examples are identified as true continuum manipulators and demonstrate a broad range of features and abilities [3].

A prime example of a continuum arm capable of dexterous behavior in nature is the octopus arm [4]. Many bio-inspired models have been proposed to simulate octopus arm features. Yekutieli *et al.* presented a dynamic model for octopus tentacles to analyze movement control and simulate 2D movements [5]. Zheng *et al.* proposed a 3D model for simulating octopus arm movements [6]. Both models take a multi-segmented approach with point masses and include longitudinal, and transverse muscles. These models demonstrate variable stiffness based on iso-volumetric property of the octopus arms, and incorporate hydrodynamic effects (drag, lift and buoyancy) for underwater operation.

These biomimetic models help to understand and analyze the biomechanical principles of octopus arms. But given state

Isuru S. Godage, David T. Branson, Emanuele Guglielmino, Gustavo A. Medrano-Cerda, and Darwin G. Caldwell are with the Istituto Italiano di Tecnologia, Department of Advanced Robotics, Via Morego 30, 16163 Genova, Italy. {isuru.godage; david.branson; emanuele.guglielmino; gustavo.cerda; darwin.caldwell}@iit.it

This work was in part supported by the European Commission in the ICT-FET OCTOPUS Integrating Project, under contract n. 231608.

of the art technology, it is not feasible to develop actual robotic prototypes to experiment and validate such biologically inspired models. Therefore these models have limited practical applications. However, there have been a number of attempts to replicate continuum arms such as large degree of freedom open serial link robotic arms [7], [8], cable/tendon driven robotic arms [9], and pneumatic/hydrostatic artificial muscle actuated arms [10], [11], among others.

Artificial muscle actuated (also variable length) multisec-tion continuum arms demonstrate strong potential to continuum robotic arms exhibiting smooth bending, extensibility/contractility, and scalability. Kinematic model proposed in [12] by Jones *et al.* describes a typical single arm section of these continuum robots (Fig. 1a). However, due to highly nonlinear and complex resulting expressions, the model serves limited purpose in dynamic analysis. Further, the use of bending curvature prevents modeling pure elongation/contraction movements (i.e., zero curvature or $l_1 = l_2 = l_3$) and produces unreliable results near singularities [11]. Thus, not many dynamic models and control strategies were developed for this class of continuum arms. But there are several inspiring works that have been carried out.

Tatlicioglu *et al.* present a planar dynamic model for multisec-tion continuum arms based on section lengths (d) and curvatures (k) [13]. However, these parameters are used independently and do not capture the geometrically coupled nature as derived in [12]. This can lead to mechanically impossible curve-length combinations. Therefore, the validity of control attempts such as [14] using this model is questionable. Also, the model assumes non-zero section curvatures and thus straight arm movements cannot be modeled.

Godage *et al.* propose a shape function-based 3D dynamic model for a prototype continuum arm developed for underwater operation [11]. It solves the singularity issues associated with previous curvature-based models and produces correct results for pure extension/contraction, and bending. To impose actuator mechanical limits, it introduces a stiffness control method. But the model assumes distributed point masses along the neutral axis, and does not include hydrodynamic forces. Also, stiffness control is unidirectional, i.e., extending actuators only have an upper limit (l_{max}), but no lower limit at $l_i = 0$ and this may result in $l_i < 0$ during simulations.

This paper seek to unify features of underwater biomimetic continuum arm models (such as hydrodynamic forces) with practical continuum robots discussed in [10], [11] to present an improved 3D dynamical model for continuum robotic

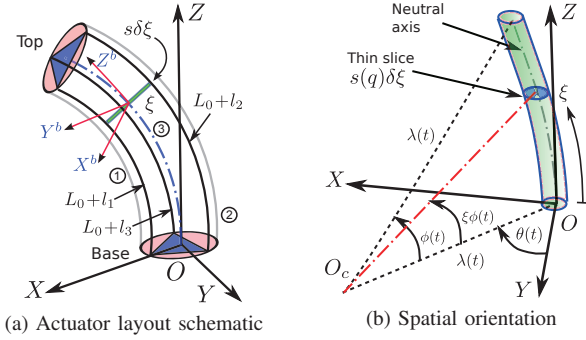


Fig. 1: Single continuum arm section

arms used in underwater operation. The model is based on the methods presented in [11] employing the mode shape function (MSF) based approach proposed in [15]. The use of MSF eliminates singularity problems, simplifies the model, and thus allows incorporating complicated underwater effects such as drag, lift, gravity, and buoyancy forces along with distributed mass, angular moments, linear forces. It also features an improved stiffness-based algorithm to include actuator mechanical limits. For improved performance and usability, a PID feedback controller in the joint space is also implemented. Further, this model can be generalized to incorporate any external force rendering its appeal to a broad spectrum of variable length geometrically constrained continuum arm configurations.

The structure of this paper is as follows. Section II briefs the prototype and the system model and section III presents the Lagrangian formulation of the continuum arm. The equations of motion are then presented in section IV along with calculation of hydrodynamic effects. Section V describes the control system design followed by conclusions in section VI.

II. METHODOLOGY

A. Introduction: Prototype Description

A prototype of the multisection continuum robotic arm is shown in Fig. 2a. It consists of three single arm sections, each with three variable length hydraulic muscle actuators (HMA) in extending mode that are mechanically constrained to actuate parallel to the neutral axis (Fig. 1a). They are fixed to circular rigid end plates at a radius r and 120° apart [11].

B. System Model: Background

For simplicity, only a single arm section is considered in the dynamic model but can be extended to multiple sections using the methods presented in [15]. In operation, the arm section bends in an arc shape defined by parameters curvature radius λ , angle subtended by the arc ϕ , and angle of the bending plane relative to the $+X$ axis θ in the spatial coordinate frame ($OXYZ$ in Fig. 1b) [11]. The actuator length changes define the joint space vector, $\mathbf{q} = \{[l_1(t) \ l_2(t) \ l_3(t)]^T : \mathbf{q} \in \mathbb{R}^3\}$ for the given arm section. The length of any i^{th} actuator is $L_0 + l_i(t)$ where L_0 is the original actuator length and $l_i(t) \in [l_{min}, l_{max}]$.

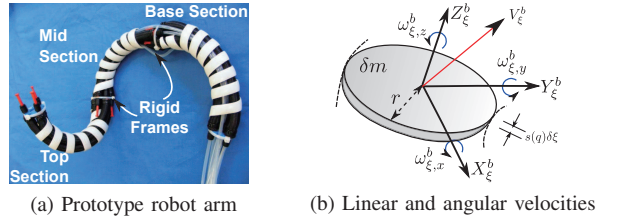


Fig. 2

Therefore both extending ($l_{min} = 0; l_{max} \in \mathbb{R}^+$) and contracting ($l_{min} \in \mathbb{R}^-; l_{max} = 0$) actuators can be modeled with appropriate mechanical limits.

C. Modal Transformation Matrix

A continuum arm has infinitely many homogeneous transformation matrices to relate body coordinate frames (BCF) to spatial coordinate frame (SCF), which can be derived as a continuous transformation matrix.

Consider a moving BCF ($O^bX^bY^bZ^b$ in Fig. 1a) along the neutral axis. Using the orientation parameters, $\{\lambda, \phi, \theta\}$, noted above, the homogeneous transformation matrix, $\mathbf{T} \in \mathbb{R}^{4 \times 4}$, for the BCF at ξ is given by (1) where $\mathbf{R}_z, \mathbf{R}_y$ are homogeneous rotational matrices about the Z and Y axes. \mathbf{P}_x is the homogeneous translation matrix along the X axis and $\xi \in [0, 1]$ is a scalar [15].

$$\begin{aligned} \mathbf{T}(\xi, \mathbf{q}) &= \mathbf{R}_z(\theta)\mathbf{P}_x(\lambda)\mathbf{R}_y(\xi\phi)\mathbf{P}_x(-\lambda)\mathbf{R}_z^T(\theta) \\ &= \begin{bmatrix} \mathbf{R}(\xi, \mathbf{q}) & \mathbf{p}(\xi, \mathbf{q}) \\ \mathbf{0} & 1 \end{bmatrix} \end{aligned} \quad (1)$$

MSFs are then derived for each element of \mathbf{T} using multivariate Taylor series expansion for joint space variables at $\mathbf{0}$ (truncation order 8) to obtain the modal transformation matrix (MTM), \mathbf{T}_Φ , in (2) where $\Phi_R \in \mathbb{R}^{3 \times 3}$ and $\phi_p \in \mathbb{R}^3$ are modal rotation matrix and modal position vector respectively [15]. These MSFs are multivariate polynomials with positive exponents and defined even for straight sections thus circumventing the singularity problems associated with previous models [11].

$$\mathbf{T}_\Phi(\xi, \mathbf{q}) = \begin{bmatrix} \Phi_R(\xi, \mathbf{q}) & \phi_p(\xi, \mathbf{q}) \\ \mathbf{0} & 1 \end{bmatrix} \quad (2)$$

III. LAGRANGIAN FORMULATION

To derive the equations of motion, classical Lagrangian formulation is used [16]. Unlike rigid bodies, this continuum section has a variable mass (m). It is assumed to be made up with an infinite number of thin circular slices as shown in Fig. 1. Kinetic and potential energies are calculated for a slice at ξ . Total energy is then determined by integrating the energies from base to top ($\xi : 0 \rightarrow 1$).

A. Mass of a Thin Slice

The mass of a pneumatic muscle actuator can be assumed constant neglecting the air mass. But the arm under investigation uses water operated HMAs. Therefore, the arm section has a variable mass given in (3) where m_0 and m_w

are construction material mass and water mass respectively. A detailed derivation can be found in [11]. The volume density of the arm section, ρ_v , in (4) is assumed uniform, and therefore, the center of gravity of a thin slice is at the geometric center.

$$m(\mathbf{q}) = m_0 + m_w(\mathbf{q}) \quad (3)$$

$$\rho_v(\mathbf{q}) = m(\mathbf{q}) V(\mathbf{q})^{-1} = m(\mathbf{q}) \{A s(\mathbf{q})\}^{-1} \quad (4)$$

where V is the section volume, A is the section cross section area, and $s(\mathbf{q}) = \lambda(\mathbf{q}) \phi(\mathbf{q})$ is the length of the neutral axis. Having defined the section density, the mass of any slice is derived in (5) where δV is the slice volume.

$$\begin{aligned} \delta m(\mathbf{q}) &= \rho_v(\mathbf{q}) \delta V(\mathbf{q}) = \rho_v(\mathbf{q}) \{A s(\mathbf{q}) \delta \xi\} \\ &= \rho_v(\mathbf{q}) V(\mathbf{q}) \delta \xi = m(\mathbf{q}) \delta \xi \end{aligned} \quad (5)$$

With the variable slice mass, the inertial matrix, $\delta \mathcal{M}(\mathbf{q}) = \delta m(\mathbf{q}) \cdot \text{diag} \{1, 1, 1, \frac{1}{4}r^2, \frac{1}{4}r^2, \frac{1}{2}r^2\} \in \mathbb{R}^{6 \times 6}$, can be derived for a thin slice with respect to the BCF where r is the slice radius.

B. Kinetic Energy

Velocity for a slice at ξ of the arm is first derived for calculating the kinetic energy. Total kinetic energy is then determined by integrating the slice kinetic energy along the length of the arm.

1) Slice Velocity and Kinetic Energy: Using the MTM obtained in (2), instantaneous body velocity, $\mathbf{V}_\xi^b \in \mathbb{R}^6$, for a slice at ξ is derived in (6) where $\mathbf{v}_\xi^b \in \mathbb{R}^3$ is the linear velocity of the center of mass, $\omega_\xi^b \in \mathbb{R}^3$ is the angular velocity about the respective body coordinate axes, and $\mathbf{J}_\xi^b \in \mathbb{R}^{6 \times 3}$ is the Modal body Jacobian matrix [17]. Dependency variables have been dropped for brevity.

$$\mathbf{V}_\xi^b(\mathbf{q}, \dot{\mathbf{q}}) = \begin{bmatrix} \mathbf{v}_\xi^b \\ \omega_\xi^b \end{bmatrix} = \begin{bmatrix} \Phi_R^T \dot{\Phi}_p \\ (\Phi_R^T \dot{\Phi}_R)^\vee \end{bmatrix} = \mathbf{J}_\xi^b(\mathbf{q}) \dot{\mathbf{q}} \quad (6)$$

Having defined body velocity, the kinetic energy of a slice, δK , along the arm is defined as

$$\begin{aligned} \delta K(\mathbf{q}, \dot{\mathbf{q}}) &= \frac{1}{2} (\mathbf{V}_\xi^b)^T \delta \mathcal{M}(\mathbf{q}) (\mathbf{V}_\xi^b) \\ &= \frac{1}{2} (\mathbf{J}_\xi^b \dot{\mathbf{q}})^T \delta \mathcal{M}(\mathbf{q}) (\mathbf{J}_\xi^b \dot{\mathbf{q}}) \end{aligned} \quad (7)$$

2) Total Kinetic Energy: The total kinetic energy, K , is then calculated by integrating all slice kinetic energies as

$$K(\mathbf{q}, \dot{\mathbf{q}}) = \int_0^1 \delta K(\mathbf{q}, \dot{\mathbf{q}}) d\xi = \frac{1}{2} \dot{\mathbf{q}}^T \mathbf{M}(\mathbf{q}) \dot{\mathbf{q}} \quad (8)$$

where

$$\mathbf{M}(\mathbf{q}) = \int_0^1 \{ (\mathbf{J}_\xi^b)^T \delta \mathcal{M}(\mathbf{q}) (\mathbf{J}_\xi^b) \} d\xi$$

C. Potential Energy

Three types of potential energy are present in the system. Potential energy due to gravity and buoyancy (P_{gb}), elastic potential energy (P_e), and bending potential energy (P_b).

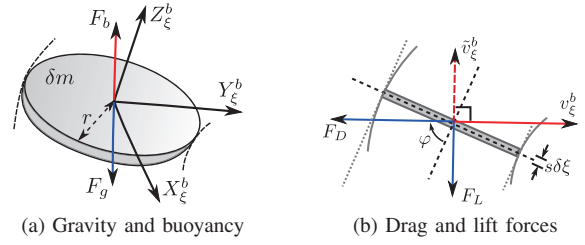


Fig. 3: External forces affecting the slices

1) Gravitational and Buoyant Potential Energy: On a slice at ξ , the buoyancy force, δF_b^s , acts in opposition to the gravity force, δF_g^s (Fig. 3a) and the net force is given by (9) where $\mathbf{g}^s = [0 \ 0 \ g]^T$ is the gravity vector in SCF and ρ_w is the density of water. Now the potential energy of a slice due to gravity and buoyancy, δP_{gb} , is given in (10) where $\mathbf{g}_e^s = (1 - \rho_w \rho_v^{-1}) \mathbf{g}^s$ is the effective gravity.

$$\begin{aligned} \delta F_{gb}^s(\mathbf{q}) &= \delta F_g^s(\mathbf{q}) - \delta F_b^s(\mathbf{q}) \\ &= \rho_v(\mathbf{q}) (V(\mathbf{q}) \delta \xi) \mathbf{g}^s - \rho_w (V(\mathbf{q}) \delta \xi) \mathbf{g}^s \end{aligned} \quad (9)$$

$$\delta P_{gb}(\mathbf{q}) = \rho_v(\mathbf{q}) (V(\mathbf{q}) \delta \xi) \phi_p^T \mathbf{g}_e^s = (m \delta \xi) \phi_p^T \mathbf{g}_e \quad (10)$$

Total potential energy due to gravity and buoyancy, P_{gb} , of the arm is determined as

$$P_{gb}(\mathbf{q}) = \int_0^1 (\delta P_{gb}(\mathbf{q})) d\xi = m(\mathbf{q}) \left(\int_0^1 \phi_p^T d\xi \right) \mathbf{g}_e^s \quad (11)$$

2) Elastic and Bending Potential Energy: The elastic and bending potential energy of the arm section is mainly due to expansion and deformation of the Silicone tubes. The total elastic potential energy is expressed in (12) where $\mathbf{K}_e = \text{diag} \{K_{e1}, K_{e2}, K_{e3}\}$ is the elastic stiffness matrix of the joint space and K_{ei} are the elastic stiffness coefficients of the three HMAs. Therefore, individual actuator mechanical limits (l_{min}, l_{max}) can be defined via stiffness coefficients as given in (13) where k_1 and k_2 are assumed constant and $k_1 \ll k_2$.

$$P_e(\mathbf{q}) = \frac{1}{2} \mathbf{q}^T \mathbf{K}_e \mathbf{q} \quad (12)$$

$$K_{ei} = \begin{cases} k_1 & : l_{min} \leq l_i \leq l_{max} \\ k_2 & : l_{max} < l_i \text{ OR } l_i < l_{min} \end{cases} \quad (13)$$

The bending potential energy of the arm section is proportional to the square of bending angle ϕ , (Fig. 1b) and expressed in (14) where K_b is the bending stiffness coefficient of the arm which is assumed constant [11].

$$P_b(\mathbf{q}) = \frac{1}{2} K_b \left(\frac{\phi}{2} \right)^2 \quad (14)$$

3) The Lagrangian: Substituting results from (8), (11), (12), and (14) the Lagrangian, L , of the system is defined by (15) where $P = P_{gb} + P_e + P_b$ is the total potential energy.

$$L = K - P \quad (15)$$

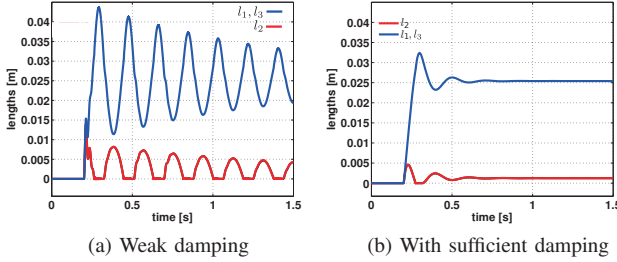


Fig. 4

IV. EQUATIONS OF MOTION

Utilizing the Lagrangian derived in (15), the equations of motion in the joint space for the continuum arm are obtained in matrix form as

$$\mathbf{M}(\mathbf{q}) \ddot{\mathbf{q}} + \mathbf{C}(\mathbf{q}, \dot{\mathbf{q}}) \dot{\mathbf{q}} + \mathbf{G}(\mathbf{q}) = \boldsymbol{\tau}_e \quad (16)$$

where $\mathbf{M} \in \mathbb{R}^{3 \times 3}$ is the generalized mass matrix, $\mathbf{C} \in \mathbb{R}^{3 \times 3}$ is the centrifugal and Coriolis forces matrix, \mathbf{G} is the conservative forces vector, and $\boldsymbol{\tau}_e \in \mathbb{R}^3$ is the input force vector in the joint space [18]. Physically, $\boldsymbol{\tau}_e$ is the force generated by elongating HMAs due to the hydraulic pressure input. For generalizing the proposed model, only actuator length parameters are considered. However other model variables (i.e., tensile forces in tendons and pressure in HMAs) can be included with additional transformations as discussed in [12].

A. Inherent System Damping

The composite continuum arm section exhibits considerable damping in operation. This is due to friction forces generated between the Silicone tubes and the braided nylon sleeves, and between the actuators as a result of relative length changes. Without accounting for these energy losses and buoyancy effect, the step response of the system (obtained by providing a step input to one PMA of the arm) in (16) is shown in Fig. 4a. It shows slowly decaying highly oscillatory response. Therefore, an additional damping term, $\mathbf{D}_F \dot{\mathbf{q}}$ is added to (16) where $\mathbf{D}_F = \text{diag}\{15, 15, 15\}$, to accommodate for inherent system damping as a reasonable first approximation. The step response for the sufficiently damped system is shown Fig. 4b. Errors due to these unmeasured friction and model imperfections can be compensated via feedback control as discussed in section V for improved reference signal tracking [19].

B. External Forces: Hydrodynamic Drag and Lift

The hydrodynamic drag and lift forces are developed during underwater arm movements. However, the theory of fluid dynamics is rather complex, and it is difficult to develop a reliable model for most hydrodynamic effects. In this case, unlike classical fluid dynamic analysis, fluid resistance cannot be calculated taking the entire continuum arm because; (i) velocity is nonlinear across the arm (ii) changing arm shape. Therefore firstly, the fluid resistance force is found for a band of $s\delta\xi$ thickness at ξ , in the

BCF. The slice drag force, δF_D^b , is parallel to the body velocity \mathbf{v}_ξ^b and calculated in (17) where $\delta A = \pi r s \delta \xi$ is the effective area facing the fluid flow and C_D is the drag coefficient (Fig. 3b). The lift force, δF_L^b , acting perpendicular to drag force is given by (18) where $\tilde{\mathbf{v}}_\xi^b$ is a velocity vector defined perpendicular to body velocity with $\|\tilde{\mathbf{v}}_\xi^b\| = \|\mathbf{v}_\xi^b\|$, and C_L is the lift coefficient [20]. The linear velocity of slice is used to calculate drag and lift forces since the angular velocity contribution is negligible. Also, coefficients C_D and C_L depend on the flow incidence angle φ (Fig. 3b) and determined from approximated polynomial relationships during simulations [21].

$$\delta F_D^b(\mathbf{q}, \dot{\mathbf{q}}) = -0.5 \rho_w \delta A C_D \left\{ (\mathbf{v}_\xi^b)^T \mathbf{v}_\xi^b \right\} \frac{\mathbf{v}_\xi^b}{\|\mathbf{v}_\xi^b\|} \quad (17)$$

$$\delta F_L^b(\mathbf{q}, \dot{\mathbf{q}}) = -0.5 \rho_w \delta A C_L \|\mathbf{v}_\xi^b\| \mathbf{v}_\xi^b \quad (18)$$

Hydrodynamic drag and lift force effects in the joint space, $\boldsymbol{\tau}_{DL}$, is then calculated by transforming the net fluid resistance force in the BCF using \mathbf{J}_ξ^b , as

$$\begin{aligned} \boldsymbol{\tau}_{DL} &= (\mathbf{J}_\xi^b)^T \{ \delta F_D^b + \delta F_L^b \} \\ &= -0.5 \rho_w \delta A \|\mathbf{v}_\xi^b\| (\mathbf{J}_\xi^b)^T (C_D \mathbf{v}_\xi^b + C_L \tilde{\mathbf{v}}_\xi^b) \end{aligned} \quad (19)$$

The total fluid resistance is then determined in (20) by integrating $\boldsymbol{\tau}_{DL}$ along the arm. The drag and lift forces due to the top plate of the arm, $\boldsymbol{\tau}_{DL,top}$, is given by (21) where $A_{top} = \pi r^2$, \mathbf{J}_1^b is the modal Jacobian matrix, \mathbf{v}_1^b and $\tilde{\mathbf{v}}_1^b$ are linear velocity terms, all evaluated at $\xi = 1$.

$$\boldsymbol{\tau}_{DL} = \int_0^1 \delta \boldsymbol{\tau}_{DL} d\xi \quad (20)$$

$$\boldsymbol{\tau}_{DL,top} = -0.5 \rho_w A_{top} \|\mathbf{v}_1^b\| (\mathbf{J}_1^b)^T (C_D \mathbf{v}_1^b + C_L \tilde{\mathbf{v}}_1^b) \quad (21)$$

Note that, apart from the singularity problems in previous curvature-based continuum arm models ([12], [13]), it is not feasible to include nonlinear external effects such as hydrodynamic forces due to prohibitively complex resulting expressions. But, as shown in this section, the modal approach facilitates simplified and straight forward formulation of such forces. This result can be extended to incorporate any external force acting on variable length continuum arms by transforming to the joint space using modal body Jacobian, \mathbf{J}_ξ^b , and spatial Jacobian \mathbf{J}_ξ^s . Also, the resulting integrals are independent of time and hence readily precomputed leading to computational efficiency in dynamic simulations.

C. Final Equation of Motion

Combining (16), (20), and (21) the underwater dynamic system is represented in (22) where $\boldsymbol{\tau}_D = \boldsymbol{\tau}_{DL} + \boldsymbol{\tau}_{DL,top}$. Dependency variables are dropped for brevity.

$$\mathbf{M} \ddot{\mathbf{q}} + \mathbf{C} \dot{\mathbf{q}} + \mathbf{D}_F \dot{\mathbf{q}} + \mathbf{G} = \boldsymbol{\tau}_e + \boldsymbol{\tau}_D \quad (22)$$

TABLE I: PARAMETER NUMERICAL VALUES

Param	Value	Unit	Param	Value	Unit
L_0	0.15	m	r	0.009	m
l_{min}	0	m	l_{max}	0.044	m
m_0	0.05	kg	g	9.81	ms^{-2}
ρ_w	1000	kgm^{-3}	K_b	0.1	$kgm^2 s^{-2} rad^{-1}$
k_2	10^6	kgs^{-2}	k_1	700	kgs^{-2}

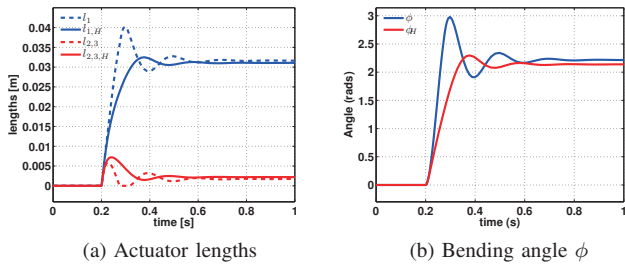


Fig. 5: Open loop step response and hydrodynamic effects

D. Underwater Effects and Open Loop Step Response

Numerical simulations are carried out to investigate hydrodynamic effects on the continuum arm. Parameter values listed in Table I are used for numerical simulations.

A comparison is made on the effect of hydrodynamic forces on the continuum arm employing open loop systems with and without the hydrodynamic effects described in (22) and (16). A step input, starting from $t = 0.2s$ of $\tau_e = [25 \ 0 \ 0]^T$ is applied to both models and responses for length changes (l_i) and bending angles (ϕ) are shown in Fig. 5a and Fig. 5b where subscript H stands for underwater system output. This causes the arm section to bend suddenly and tends to oscillate and the results are visually compared in the video at [22]. It clearly indicates that hydrodynamic effects significantly dampen the submerged arm compared to the results without hydrodynamic effects, exhibiting less length overshoot (6.9% vs. 25.66%), bending angle overshoot (4.34% vs. 21.34%), and transient oscillations. Also note the residual passive actuation of other HMAs (l_2, l_3) due to geometrically constrained coupling of the actuators. The steady state output difference is the result of buoyant forces acting on the continuum arm against bending.

V. CONTROL DESIGN

For better utilization of variable length continuum arms, they should be controllable with bounded control signals, i.e., pressure for PMA/HMAs and tensile forces for cables. But to the best of authors knowledge, without complete 3D dynamic models to accurately describe these robots such as [10], dynamic control has not been possible.

However, the proposed dynamic model is based on accurate kinematic representation of variable length continuum robots [12] and it enables implementing control schemes for accurate control. As seen in Fig. 5, the open loop system in (22) has undesirable gain, rise time, and settling time. To improve the system performance, classical PID feedback control is implemented in the joint space (Fig. 6). For the

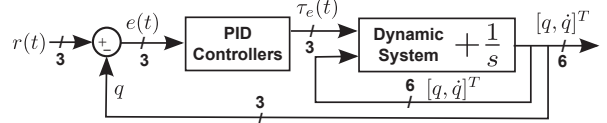


Fig. 6: PID Controller

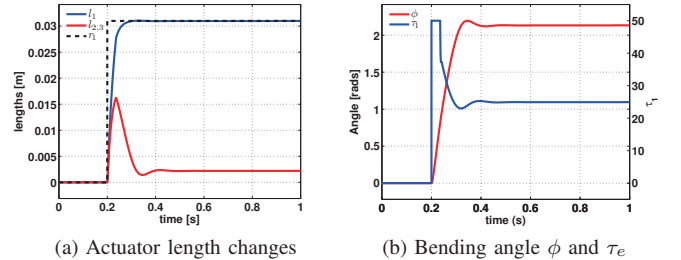


Fig. 7: Closed loop step response

prototype under consideration, this refers to the actuator lengths (l_i) where the feedback can be obtained by measuring actuator lengths with, for instance, string encoders.

The control input force for i^{th} actuator (τ_i) for tracking a reference signal (r_i) is given by (23) where $e_i = r_i - q_i$ is the tracking error, $K_p = 2 \times 10^4$, $K_i = 4 \times 10^4$, and $K_d = 10^2$ are the tuned proportional, integral and derivative coefficients respectively. Numerical results on step response, pure elongation, and bending with bounded lengths are presented in section V-A to validate the design.

$$\tau_{e,i}(t) = K_P e_i(t) + K_I \int_0^n e_i(\eta) d\eta + K_D \frac{de_i(t)}{dt} \quad (23)$$

A. Closed Loop Step Response

The system is given a step input reference signal to actuator one $r_1(t)$, with bounded control input ($\tau_e \in [0, 50]$ is analogous to operating pressure range) and response for length changes is shown Fig. 7a. Bending angle (ϕ) and controlled input force (τ_e) are shown in Fig. 7b. Similar to open loop response, this causes the arm to bend and a visual comparison is made with the open loop response at [22] to show the controlled smooth bending. Improved system response is observed in contrast to open loop results in section IV-D, with zero length overshoot, faster settling time (0.1s vs. 0.4s) and rise time (0.06s vs. 0.12s). The bending overshoot is due to uncontrollable momentary passive extension of other actuators (l_2, l_3) and this would need a negative pressure for extending HMAs whereas $\tau_e \geq 0$.

B. Pure Elongation

To achieve pure elongation, all actuators are made to track the reference signal $r(t)$, shown in Fig. 8a with actuator length changes. Bending angle ϕ and input force τ_e is illustrated in Fig. Fig. 8b. As seen on the plot, the HMAs are subject to the same length changes resulting in pure elongation verified by ϕ remaining unchanged at zero and visually illustrated in [22]. Note that this is a singular configuration in previous curvature-based models [12] yielding undefined transformation and Jacobian matrices. But the

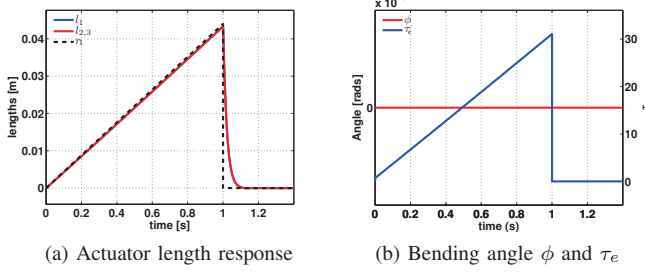


Fig. 8: Pure elongation results

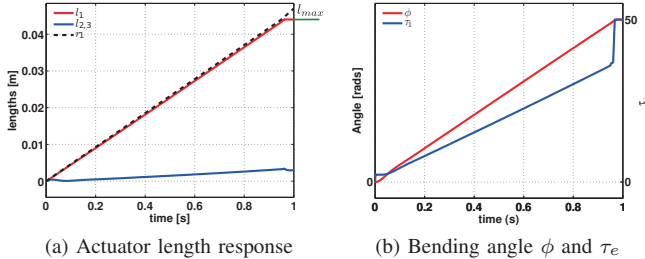


Fig. 9: Bending with constrained actuator lengths

proposed model provides correct results without numerical instabilities.

C. Bending Simulation with Actuator Mechanical Limits

An improved stiffness-based, bi-directional algorithm (in contrast to [11]), is presented in (13) and applied to the proposed model to constrain variable lengths to their operational range. To illustrate the results, actuator one is given the reference signal $r_1(t)$ and the actuator length (l_1) reaching the upper extension limit, l_{max} , can be observed in Fig. 9a. This causes the arm to reach maximum bending at a constant rate while the system trying to track r_1 with maximum control input as shown in Fig. 9b and visually at [22]. The effect of the improved bi-directional limits is observed in Fig. 5 and Fig. 9a by maintaining the actuator lengths within the operational range, i.e., $l_i(t) \in [l_{min}, l_{max}] \forall t$, thus successfully accounting for actuator mechanical limits.

VI. CONCLUSIONS

An improved 3D dynamic model for variable length continuum arms intended for underwater operation is presented. The proposed model utilizes a MSF based approach, thus avoiding the complex derivations and singularities associated with previous modeling methods, and enables the inclusion of highly nonlinear external effects such as hydrodynamic forces. The model is directly derived in the joint space and provides enhanced insight into practical aspects of operation and control of continuum arms. The comparative effect of underwater forces are graphically and visually illustrated. For better performance and usability, a PID feedback controller is implemented in the joint space and numerically validated. The proposed model successfully demonstrates underwater pure elongation and bending with the improved bi-directional actuator length constraining algorithm to yield physically

accurate results. This approach can also be generalized to model any external force acting on any variable length continuum robotic arm.

REFERENCES

- [1] G. Robinson and J. Davies, "Continuum robots-a state of the art," in *IEEE Int. Conf. on Robotics and Automation*, 1999, pp. 2849–2854.
- [2] W. M. Kier and K. Smith, "Tongues, tentacles and trunks: the biomechanics of movement in muscular-hydrostats," *Zoological Journal of the Linnean Society*, vol. 83, pp. 307–324, 1985.
- [3] D. Trivedi, C. D. Rahn, W. M. Kier, and I. D. Walker, "Soft robotics: Biological inspiration, state of the art, and future research," *Applied Bionics and Biomechanics*, vol. 5, no. 3, pp. 99–117, 2008.
- [4] W. M. Kier and M. Stella, "The arrangement and function of octopus arm musculature and connective tissue," *Journal of Morphology*, vol. 268, no. 10, pp. 831–843, 2007.
- [5] Y. Yekutieli, R. Sagiv-Zohar, R. Aharonov, Y. Engel, B. Hochner, and T. Flash, "Dynamic model of the octopus arm. i. biomechanics of the octopus reaching movement," *Journal of neurophysiology*, vol. 94, no. 2, p. 1443, 2005.
- [6] T. Zheng, D. T. Branson, E. Guglielmino, and D. G. Caldwell, "A 3D Dynamic Model for Continuum Robots Inspired by An Octopus Arm," in *IEEE Int. Conf. on Robotics and Automation*, 2011, pp. 3652–3657.
- [7] S. Hirose, *Biologically Inspired Robots: Serpentile Locomotors and Manipulators*. Oxford University Press, 1993.
- [8] G. S. Chirikjian and J. W. Burdick, "A modal approach to hyper-redundant manipulator kinematics," *IEEE Transactions on Robotics and Automation*, vol. 10, no. 3, pp. 343–354, 1994.
- [9] W. McMahan, B. A. Jones, and I. D. Walker, "Design and implementation of a multi-section continuum robot: Air-Octo," in *IEEE/RSJ Int. Conf. on Intelligent Robots and Systems*, 2005, pp. 2578–2585.
- [10] W. McMahan, V. Chitrakaran, M. A. Csencsits, D. M. Dawson, I. D. Walker, B. A. Jones, M. B. Pritts, D. Dienco, M. Grissom, and C. D. Rahn, "Field trials and testing of the OctArm continuum manipulator," in *IEEE Int. Conf. on Robotics and Automation*, 2006, pp. 2336–2341.
- [11] I. S. Godage, D. T. Branson, E. Guglielmino, G. A. Medrano-Cerda, and D. G. Caldwell, "Shape Function-Based Kinematics and Dynamics For Variable Length Continuum Robotic Arms," in *IEEE Int. Conf. on Robotics and Automation*, 2011, pp. 452–457.
- [12] B. A. Jones and I. D. Walker, "Kinematics for multiseciton continuum robots," *IEEE Trans. on Robotics*, vol. 22, no. 1, pp. 43–55, 2006.
- [13] E. Tatliciooglu, I. D. Walker, and D. M. Dawson, "New dynamic models for planar extensible continuum robot manipulators," in *IEEE/RSJ IROS*, 2007, pp. 1485–1490.
- [14] A. D. Kapadia, I. D. Walker, D. Dawson, and E. Tatliciooglu, "A model-based sliding mode controller for extensible continuum robots," in *Proceedings of the 9th WSEAS Int. Conf. on Signal processing, robotics and automation*, 2010, pp. 113–120.
- [15] I. S. Godage, E. Guglielmino, D. T. Branson, G. A. Medrano-Cerda, and D. G. Caldwell, "Novel Modal Approach for Kinematics of Multisection Continuum Arms," in *IEEE/RSJ Int. Conf. on Intelligent Robots and Systems*, 2011, pp. 1093–1098.
- [16] H. Goldstein, C. Poole, J. Safko, and S. Addison, "Classical mechanics," *American Journal of Physics*, vol. 70, p. 782, 2002.
- [17] R. M. Murray, Z. Li, S. Sastry, and S. Sastry, *A mathematical introduction to robotic manipulation*. CRC, 1994.
- [18] R. Kelly, V. Santibáñez, and A. Loría, *Control of Robot Manipulators in Joint Space*. Springer Verlag, 2005.
- [19] S. Engelberg, *A mathematical introduction to control theory*. Imperial College Pr, 2005, vol. 2.
- [20] G. Batchelor, *An introduction to fluid mechanics*. Cambridge Univ. Pr., 1967.
- [21] R. Kang, A. Kazakidi, E. Guglielmino, D. T. Branson, D. P. Tsakiris, J. A. Ekaterinaris, and D. G. Caldwell, "Dynamic Model of a Hyper-redundant, Octopus-like Manipulator for Underwater Applications," in *IEEE/RSJ Int. Conf. on Intelligent Robots and Systems*, 2011, pp. 4054–4059.
- [22] I. S. Godage. (2011) Simulation video. [Online]. Available: <http://dl.dropbox.com/u/5412272/ROBIO2011-Godage.mp4>